Supplementary Information (SI) for Journal of Materials Chemistry B.

Supporting information

Decomposable STING nanoagonist-amplified oncolytic virotherapy through remodeling the immunosuppressive microenvironment of triple-negative breast cancer

Min Mu[1,†], Guoqing Wang[2,†], Bo Chen[1], Hui Li[1], Chenqian Feng[1], Rangrang Fan[3], Nianyong Chen[1], Bo Han[4], Aiping Tong[1,*], Bingwen Zou[1,*], Gang Guo[1,*]

[1] Department of Biotherapy, Cancer Center and State Key Laboratory of Biotherapy, Department of Radiation Oncology and Department of Head and Neck Oncology, West China Hospital, Sichuan University, Chengdu, 610041, China

[2] Department of Ophthalmology, State Key Laboratory of Biotherapy, West China Hospital, Sichuan University, Chengdu, 610041, China

[3] Department of Neurosurgery, West China Hospital, Sichuan University, Chengdu, 610041, China

[4] Key Laboratory of Xinjiang Endemic Phytomedicine Resources Ministry of Education, Shihezi University College of Pharmacy, Shihezi, 832002, China

[†] These authors contributed equally to this work.

[*] Corresponding author:

E-mail address: guogang@scu.edu.cn (G. Guo) ; zoubingwen81@163.com (B. Zou); aipingtong@scu.edu.cn (A. Tong).

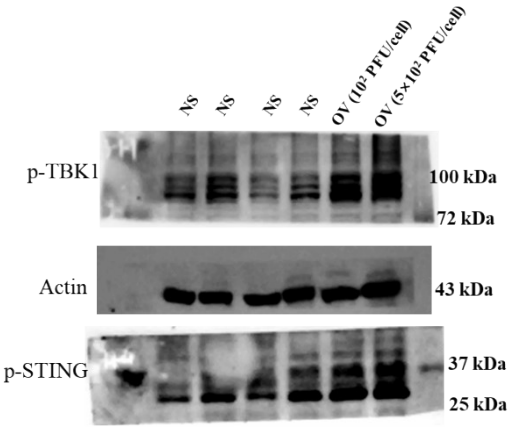

Fig. S1 WB analysis of STING pathway after treated with different dose of OVs for 24 h.

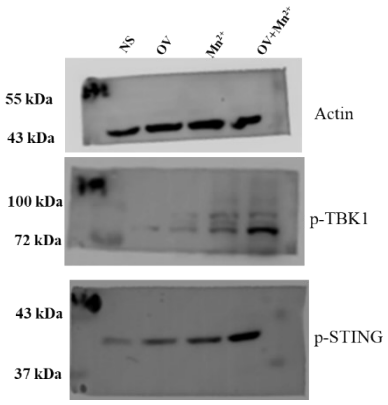

Fig. S2 WB analysis of STING pathway after treated with OV, Mn^{2+}, OV+Mn^{2+} for 24 h.

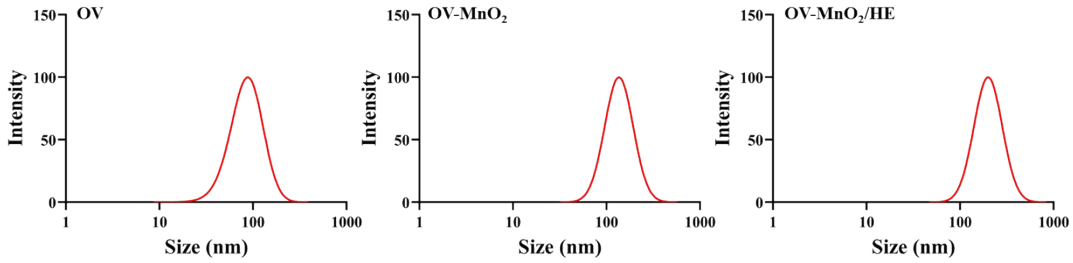

Fig. S3. The size distribution of OV, OV-MnO_2, and OV-MnO_2/HE nanoagonist by DLS.

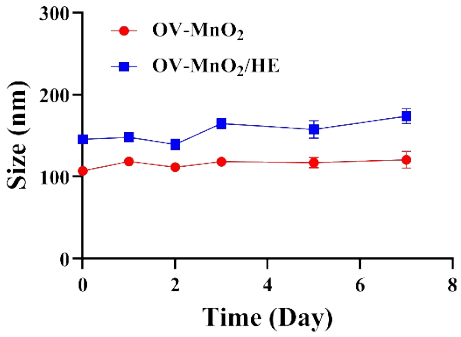

Fig. S4. The stability of OV-MnO_2 and OV-MnO_2/HE at 4 °C.

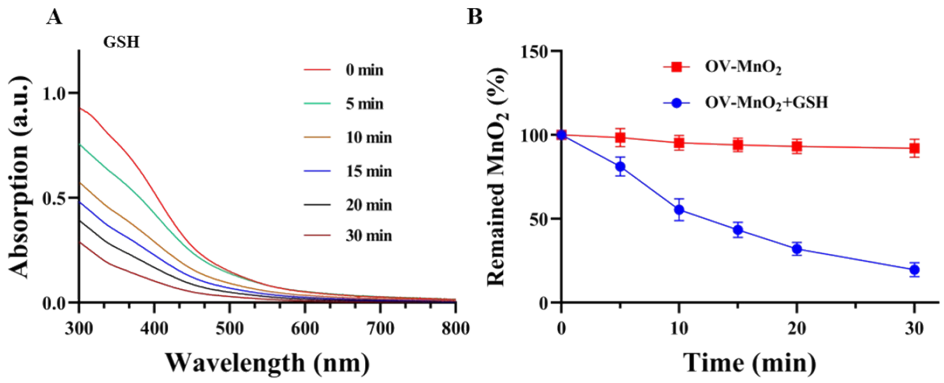

Fig. S5. Degradation behavior of OV-MnO_2 with GSH. (A) Absorption spectra of OV-MnO_2 treated with GSH at different time. (B) The degradation behavior of OV-MnO_2 dispersed water with GSH determined by the absorbance of MnO_2 at 400 nm.

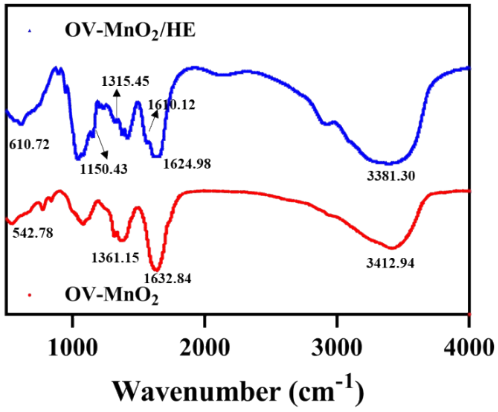

Fig. S6. FTIR spectra of OV-MnO_2 and OV-MnO_2/HE.

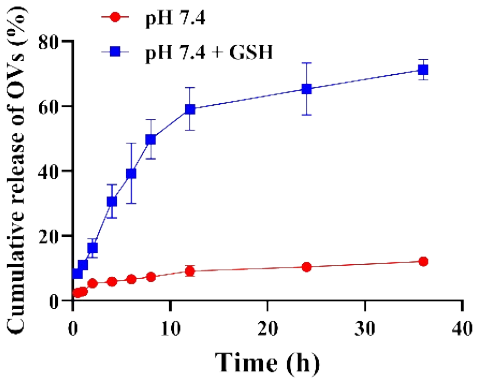

Fig. S7. OVs release profile of OV-MnO_2/HE in PBS buffer (pH 7.4) with 10 mM GSH.

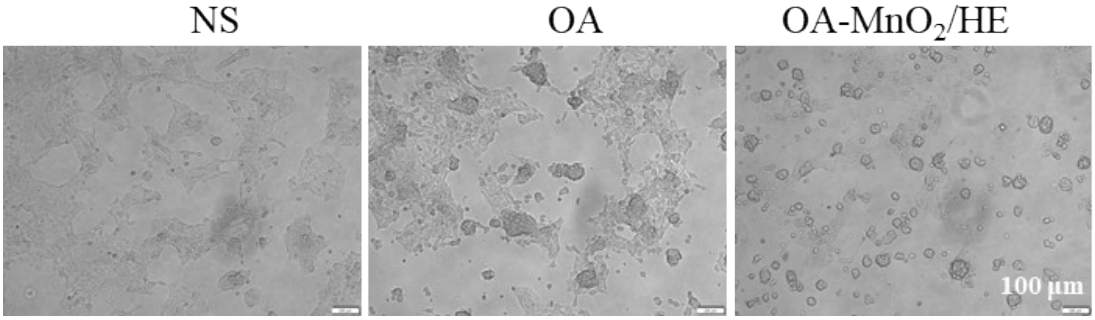

Fig. S8 Optical imaging of OV and OV-MnO_2/HE infected-4T1 cells for 48 h. Scale bar: 100 μm

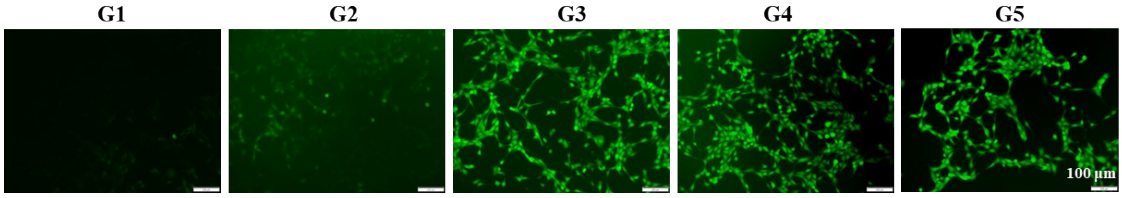

Fig. S9. The fluorescence imaging of 4T1 cells staining with H2DFCDA after different treatments. G1: NS; G2: OV; G3: MnO_2; G4: OV-MnO_2; G5: OV-MnO_2/HE. Scale bar: 100 μm

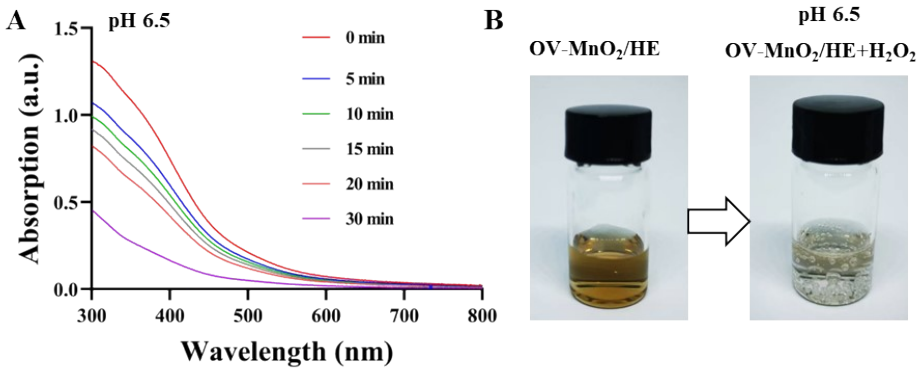

Fig. S10. (A) Absorption spectra of OV-MnO_2/HE treated pH 6.5 buffer with H_2O_2. (B) The O_2 generation ability of OV-MnO_2/HE treated pH 6.5 buffer with H_2O_2.

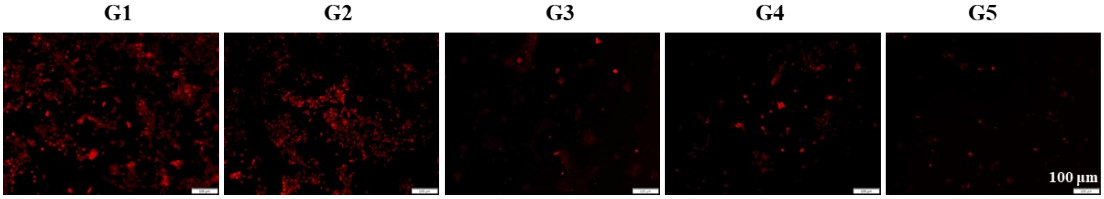

Fig. S11. The O_2 generation of 4T1 cells via [Ru(ddp)3]Cl_2 after various treatment. G1: NS; G2: OV; G3: MnO_2; G4: OV-MnO_2; G5: OV-MnO_2/HE. Scale bar: 100 μm

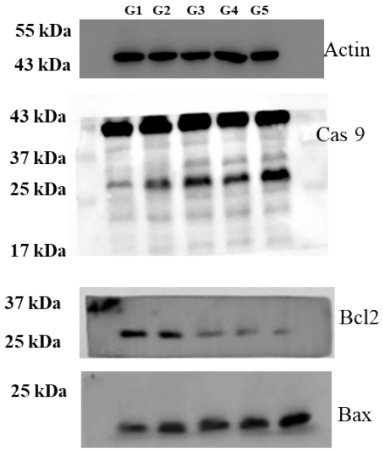

Figure S12. WB analysis for the expressions of proteins in cell apoptosis pathway in 4T1 cells. G1: NS; G2: OV; G3: MnO_2; G4: OV-MnO_2; G5: OV-MnO_2/HE.

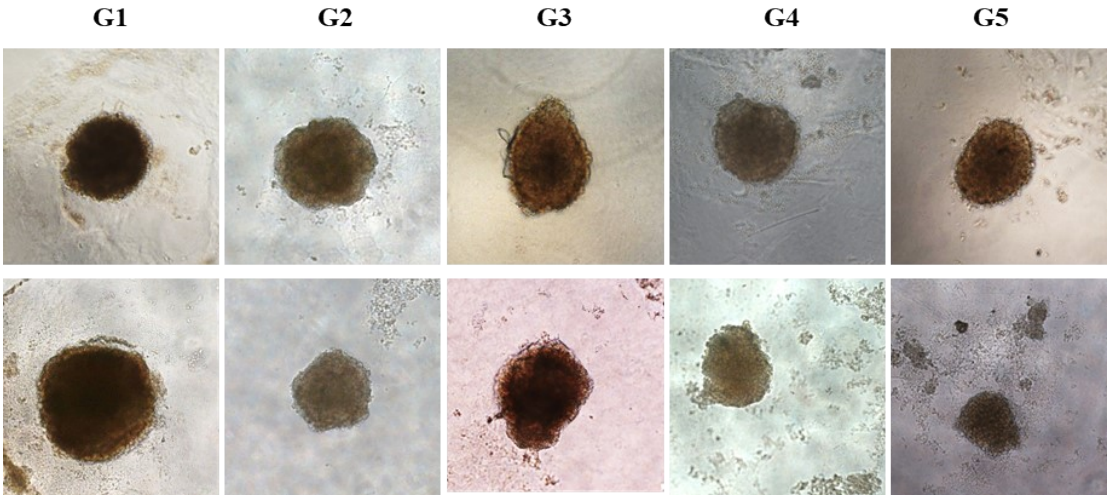

Fig. S13 The photos of 3D tumor spheroids after different treatments for 48 h. G1: NS; G2: OV; G3: MnO_2; G4: OV-MnO_2; G5: OV-MnO_2/HE

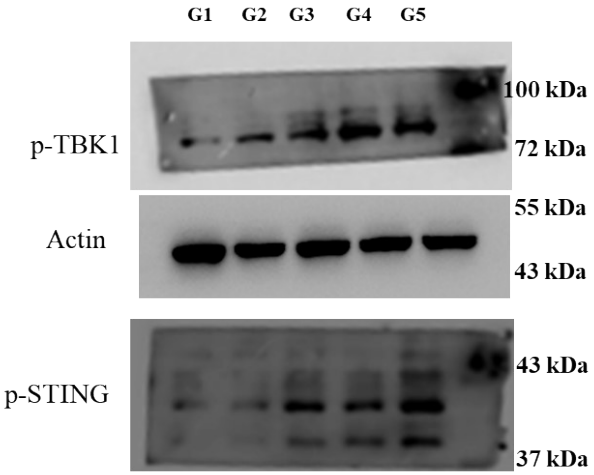

Fig. S14 WB and quantitative analysis of STING pathway proteins after incubation of 4T1/DC2.4 co-culture system with OV, MnO_2, OV-MnO_2, and OV-MnO_2/HE. G1: NS; G2: OV; G3: MnO_2; G4: OV-MnO_2; G5: OV-MnO_2/HE

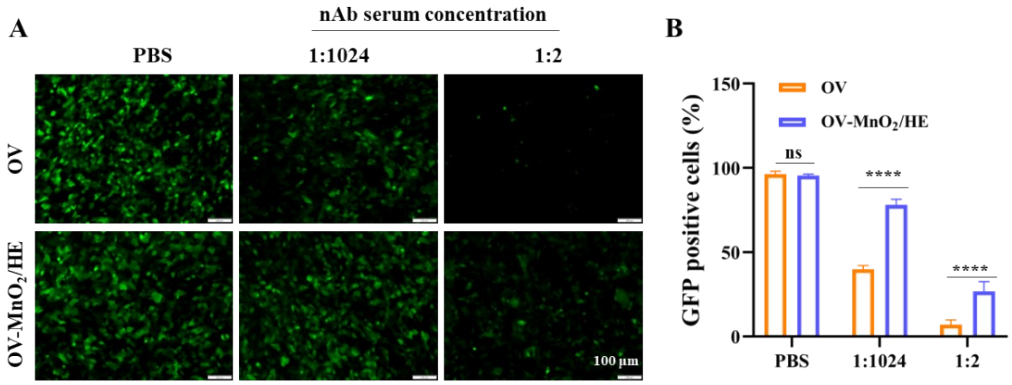

Fig. S15. Neutralization of OV and OV-MnO_2/HE in 4T1 cells was performed using anti-Ad5 serum at the specified concentrations. Scale bar: 100 μm

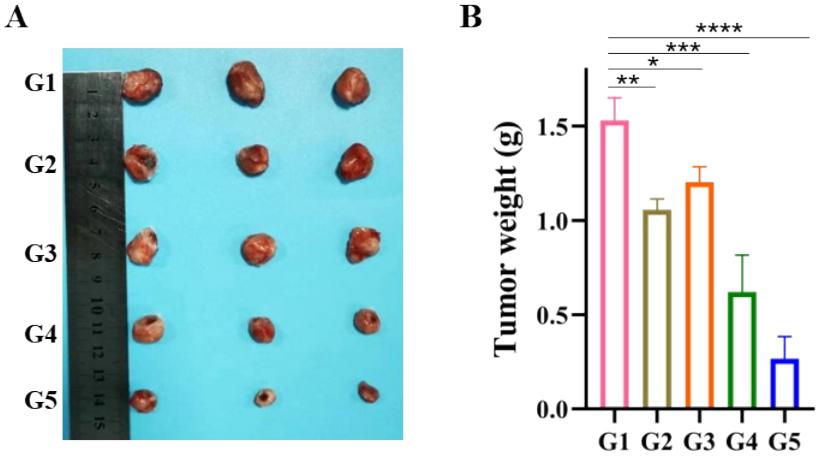

Fig. S16 The photographs (A) and weight (B) of the tumors in each group after treatment with different formulations. G1: NS; G2: OV; G3: MnO_2; G4: OV-MnO_2; G5: OV-MnO_2/HE

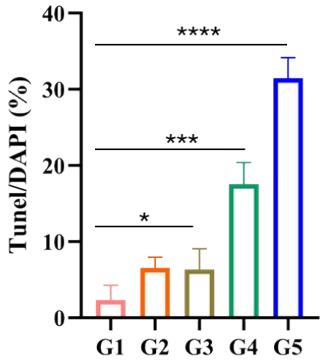

Fig. S17. The semi-quantitative fluorescence of TUNEL data.

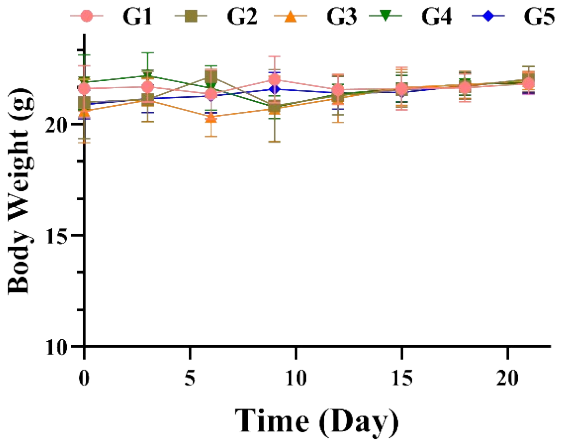

Fig. S18 Relative body weights of the mice during the treatment. G1: NS; G2: OV; G3: MnO_2; G4: OV-MnO_2; G5: OV-MnO_2/HE

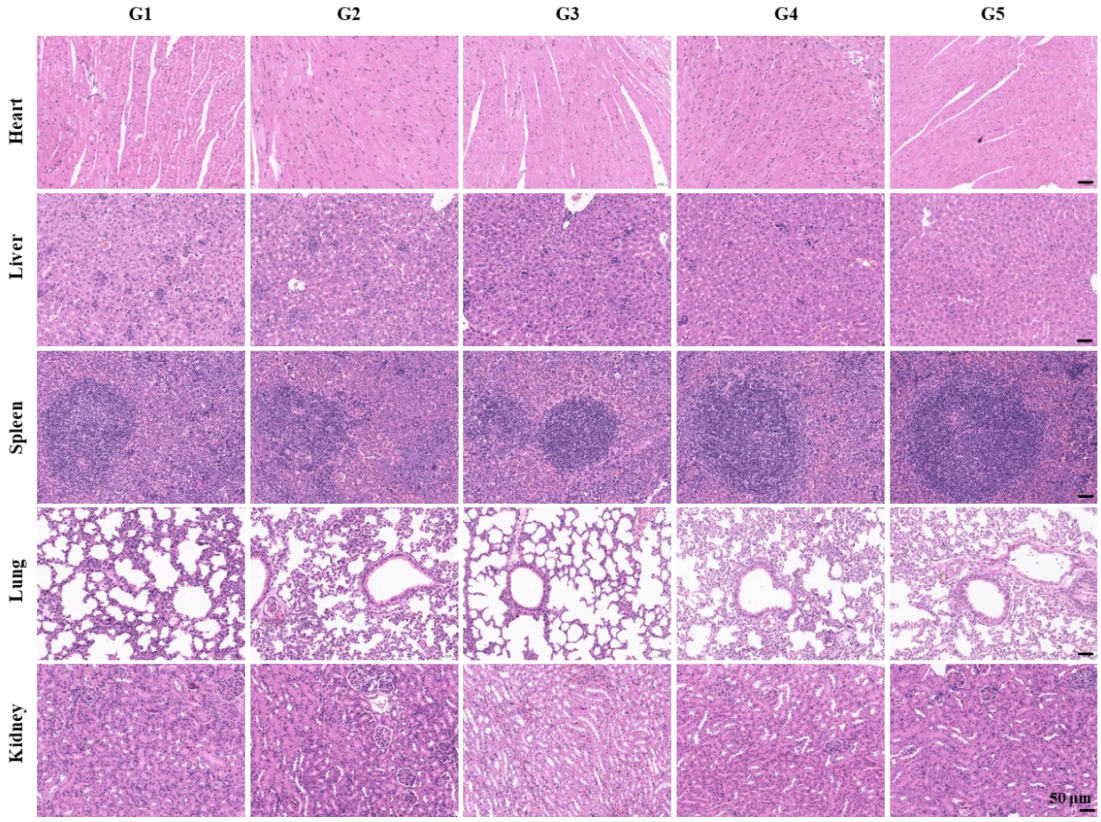

Fig. S19. HE staining of Heart, Liver, Spleen, Lung, and Kidney. G1: NS; G2: OV; G3: MnO_2; G4: OV-MnO_2; G5: OV-MnO_2/HE. Scale bar: 50 μm

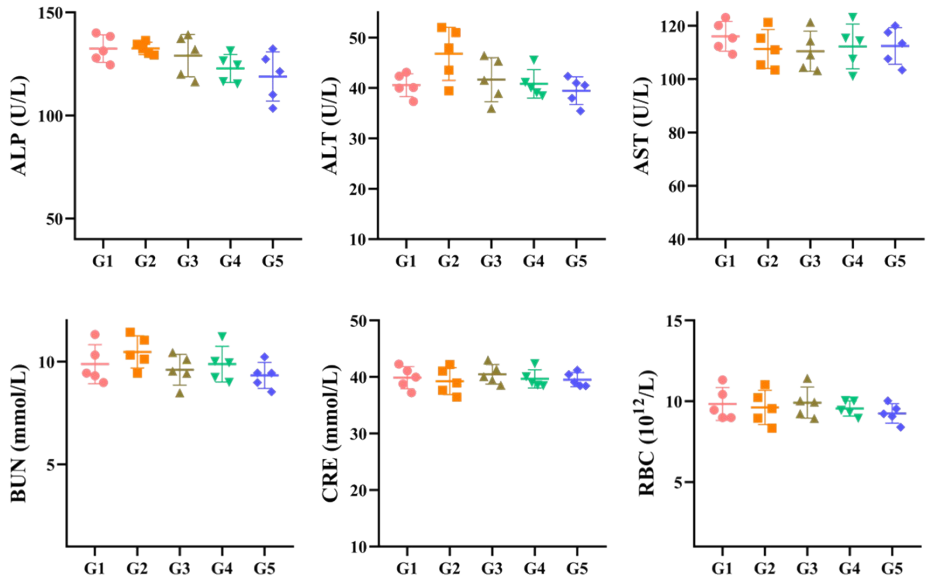

Fig. S20. Blood biochemical values of blood aspartate aminotransferase (AST), ALT, ALP, CRE, BUN, and RBC at 21 d post-injection (n = 5).

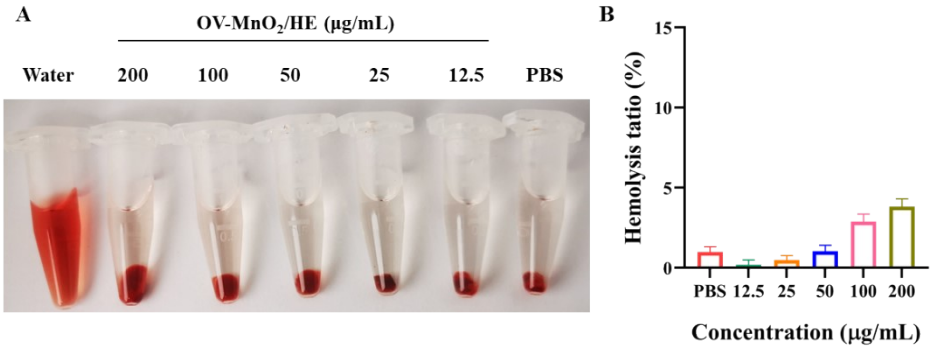

Fig. S21. The hemolysis of OV-MnO_2/HE at varied concentrations.